THE JOURNAL OF PHYSICAL CHEMISTRY LETTERS
A JOURNAL OF THE AMERICAN CHEMICAL SOCIETY

pubs.acs.org/JPCL Letter

Unraveling the Hydration Shell Structure and Dynamics of Group 10 Aqua Ions

Xin Chen,*,¶ Andres Cifuentes-Lopez,¶ Xuecheng Shao,* Lirong Lin, Demyan Prokopchuk, and Michele Pavanello*

Cite This: J. Phys. Chem. Lett. 2024, 15, 5517−5528 Read Online

ACCESS | Metrics & More | Article Recommendations | Supporting Information

ABSTRACT: We present ab initio simulations based on subsystem DFT of group 10 aqua ions accurately compared against experimental data on hydration structure. Our simulations provide insights into the molecular structures and dynamics of hydration shells, offering recalibrated interpretations of experimental results. We observe a soft, but distinct second hydration shell in Palladium (Pd) due to a balance between thermal fluctuations, metal−water interactions, and hydrogen bonding. Nickel (Ni) and platinum (Pt) exhibit more rigid hydration shells. Notably, our simulations align with experimental findings for Pd, showing axial hydration marked by a broad peak at about 3 Å in the Pd−O radial distribution function, revising the previously sharp "mesoshell" prediction. We introduce the "hydrogen bond dome" concept to describe a resilient network of hydrogen-bonded water molecules around the metal, which plays a critical role in the axial hydration dynamics.

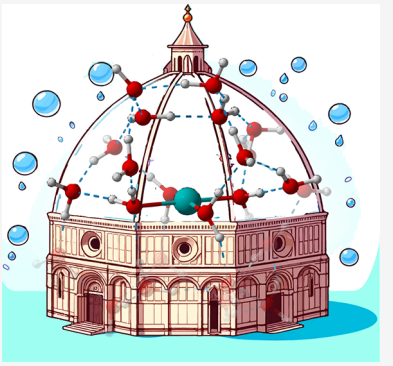

Group 10 aqua ions (i.e., $Ni^{2+}_{(aq)}$, $Pd^{2+}_{(aq)}$, and $Pt^{2+}_{(aq)}$) play critical roles in many processes in chemistry, biology, and related disciplines. For example, $Ni^{2+}_{(aq)}$ can anchor onto the interlayer of layered MnO_2 to perform as a single-ion catalyst,[1] and $Pd^{2+}_{(aq)}$ is routinely employed as catalyst in an array of chemical processes.[2] Since water is generally considered the "greenest" reaction solvent,[3] a thorough comprehension of the chemistry of group 10 aqua ions hinges on understanding the structure, dynamics, and electronic properties of the water−ion complex in aqueous solution. Because a solvation shell rearrangement is often involved in reactions, the nature of the microsolvation environment of these aqua ions has an undeniable impact on their reactivity.[4] Experimental[5,6] and theoretical[7,8] studies have thoroughly characterized the water shell structure of $Ni^{2+}_{(aq)}$. It is well-known that $Ni^{2+}_{(aq)}$ has a stable octahedral coordination shell of water molecules, the $Ni^{2+}_{(aq)}$ complex, exhibiting little dynamics[9] with a water exchange event occurring in the millisecond time scale.[10] However, $Pd^{2+}_{(aq)}$ and $Pt^{2+}_{(aq)}$ aqua ions are square planar, $[M(H_2O)_4]^{2+}$, and display a much more complex and dynamic water environment, particularly in the axial positions. To date, there are three main paradigms used for describing the axial hydration in $Pd^{2+}_{(aq)}$ and $Pt^{2+}_{(aq)}$ complexes:

- **Mesoshell.** This paradigm considers weak, symmetric coordination at the axial positions identified by a sharp peak in the M−O radial distribution function (RDF) between the first and the second solvation shell peaks located between 2.5 and 3 Å. This is supported by classical MD simulations based on force fields,[11] on empirical potential structure refinement (EPSR), and model systems that reproduce structure factors from neutron diffraction experiments, X-Ray diffraction (XRD) and extended X-Ray absorption fine structure (EXAFS).[12−14]
- **Extended first shell.** This paradigm considers the existence of axially coordinated water molecules resulting in a broad peak between the first and the second solvation shell peaks in the M−O RDF. This is supported by QM/MM simulations[15,16] and fits to EXAFS spectra of selected structures.[16]
- **"Anionic" coordination.** This paradigm was reported for some group 10 water-solvated complexes. It suggests an unusual coordination where $Pt^{2+}_{(aq)}$ is directly coordinated to a hydrogen atom of water,[17] resulting in an electrostatic attraction between the 5d orbitals and the aqua Pt ion and an axial water molecule. Quantum chemical considerations also find that weak van der Waals forces play a crucial role.[18,19]

While anionic coordination has been reported only for a limited set of complexes, the most commonly invoked paradigms for pure aqua complexes are the extended first shell and the mesoshell. For example, the mesoshell concept

Received: February 13, 2024
Revised: May 13, 2024
Accepted: May 13, 2024
Published: May 15, 2024

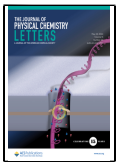

https://doi.org/10.1021/acs.jpclett.4c00464
J. Phys. Chem. Lett. 2024, 15, 5517−5528

has been advanced by several studies of the aqua Pd ion.[11−14] Unfortunately, the current understanding of the hydration shell structure and dynamics of $Pd^{2+}_{(aq)}$ is undermined for several reasons. A major obstacle has been the inability to directly probe the ion's environment experimentally, as diffraction techniques do not directly produce partial ion−water structure factors. Instead, they only provide structure factors associated with the entire system. As a result, other indirect characterization methods have been employed thus far.

One method to determine partial structure factors involves measuring the difference in diffraction data between multiple solutions of high concentration, utilizing isotopic substitutions and the differing scattering lengths of the isotopes.[20,21] This method is known to yield low signal-to-noise ratios due to the small signal contribution from the metal centers (0.5−3% of the total[22]) compared to the overwhelming signal from the solvent. Additionally, to extract partial structure factors, as demonstrated in refs 23 and 24, Monte Carlo or molecular dynamics simulations are conducted with interatomic potentials calibrated to represent the experimental data, also known as empirical potentials. However, it is important to note that there is no unique fit for these potentials regardless of whether neutron scattering or neutron scattering together with X-ray scattering data are taken as the target. In fact, it has been observed that the fits are under-determined, meaning that multiple distinct potentials can yield fits of similar accuracy.[25−27] A similar criticism can be raised for analyses of EXAFS based on few model structures rather than converged ensembles of structures[14] that may reproduce the EXAFS spectra without providing a reliable structure-to-spectrum relationship.

Early experiments (i.e., large-angle X-Ray scattering (LAXS) and EXAFS) did not predict the existence of a structured, sharp axial coordination for both $Pd^{2+}_{(aq)}$ and $Pt^{2+}_{(aq)}$ aqua ions.[28,29] Hofer et al.[16] advanced the "extended first shell" paradigm. They found a slightly improved EXAFS fit when including axial waters in the model and corroborated the finding with QM/MM simulations. However, the EXAFS fit presented in ref 16 with the axial waters is only marginally better than the one for square planar models. This shows that while a certain level of axial ligation is to be expected, the specifics of the structure (transient or stable, broad or sharp) could not be ascertained with confidence. Similar analyses were presented later for $Pd^{2+}_{(aq)}$ [14] where EXAFS results were reproduced with a fit involving only 3 structures. Bowron et al.[13] carried out a thorough analysis of several experiments (neutron and X-Ray diffration, EXAFS) applying the EPSR method (empirical potentials mentioned above) also finding a structured axial solvation for $Pd^{2+}_{(aq)}$ exemplified by a clear, sharp peak in the Pd−O RDF situated between the first and second solvation shell.

Thus, despite strong indications of identifiable axial solvation in $Pd^{2+}_{(aq)}$, the evidence pinpointing a specific structure associated with such a solvation to date remains somewhat weak. This caused a delay in the fundamental understanding of the hydration structure and dynamics of group 10 aqua ions, and specifically of the axial water coordination in $Pd^{2+}_{(aq)}$ and, to a lesser extent, of $Pt^{2+}_{(aq)}$. In this work, we aim to shed light on this process by providing an alternative interpretation for the hydration structure especially of $Pd^{2+}_{(aq)}$ that is still consistent with previous experimental results and at the same time takes into account an ensemble of structures that samples the configuration space spanned at ambient and experimental conditions.[13] Our aim is to further refine our knowledge of these systems through the lenses of ab initio molecular dynamics simulations (AIMD).[30] We still strongly and crucially rely on comparison with experimental data which provide us with an invaluable benchmark.

The main reason hindering widespread AIMD simulations of aqua ions is the need to consider large system sizes (hundreds of water molecules and large metal−counterion distances) and long simulation times (i.e., hundreds of ps). Such requirements are not easily met by standard electronic structure methods based on density functional theory (DFT) because these have a computational scaling that grows cubically with system size, i.e., $O(N^3)$. Such scaling would require significant and expensive computational resources for carrying out the simulations. There are several alternative methods to standard DFT that feature a more amenable computational scaling while retaining a satisfactory accuracy of the simulation. For example, linear scaling DFT,[31] as well as divide and conquer methods, such as the fragment molecular orbital (FMO) method[32,33] and subsystem DFT (sDFT).[34−36] Our group has focused on the development of sDFT methods which has resulted in robust, fast, and accurate sDFT software.[37−39] In the recent past, our group showed that sDFT can predict the structure of molecular liquids accurately (self-translational diffusion coefficient of water[39] and liquid carbon dioxide[40]) as it was shown to correct spurious intersubsystem charge transfer that occurs when employing semilocal exchange−correlation functionals[39,41] due to the so-called self-interaction error. The self-interaction error within each subsystem can be addressed on a case-by-case basis as needed. For example, in this work, we use the Hubbard U correction[42−44] for the metal-containing subsystem to counteract the self-interaction error locally at the metal site.[45]

After a short introduction to the computational methodology, there is a devoted presentation of the results related to uncovering a quantitative agreement between the simulations and the available experiments. We also provide an in-depth analysis of the competition between thermal fluctuations, the attraction from the bare metal centers to the water molecules, and the constraints imposed by the ensuing hydrogen bond (HB) network. The conclusions underscore the importance of our findings, prompting us to suggest a revision of the "mesoshell" paradigm to a "hydrogen bond dome" concept, which we believe is more precise.

Methods. AIMD simulations involve propagating the positions of each atom according to Newton's equations of motion in the presence of a computational thermostat that regulates the system's temperature. The forces on the atoms are computed with ab initio electronic structure methods. In this work, we use a flavor of density functional theory (DFT) known as subsystem DFT (or sDFT). The most important advantage of sDFT over DFT is its favorable computational scaling allowing the user to run long AIMD simulations for system sizes typically not accessible with standard computational resources.

sDFT can be summarized with two equations. One regards the expression of the total electron density rigorously in terms of subsystem electron densities. Namely,

$$\rho(\mathbf{r}) = \sum_{I}^{N_S} \rho_I(\mathbf{r}) \tag{1}$$

https://doi.org/10.1021/acs.jpclett.4c00464
J. Phys. Chem. Lett. 2024, 15, 5517−5528

where N_S is the total number of subsystems. ρ_I is the electron density of subsystem I. Equation 1 clearly intends to "divide and conquer" the electronic system into subsystems of smaller size than the full system.

Key to the accuracy of sDFT is the fact that subsystems interact weakly with each other. Thus, the second equation regards the energy functional which can be rigorously split into subsystem-additive and subsystem-nonadditive terms

$$E[\{\rho_I, v_{ext}^I\}] = \sum_{I=1}^{N_S} E[\rho_I, v_{ext}^I] + E^{nad}[\{\rho_I, v_{ext}^I\}] \quad (2)$$

where v_{ext} is the electron−nuclear attraction potential. The energy functional of each subsystem is defined in the usual way according to DFT. The nonadditive term, $E^{nad}[\{\rho_I, v_{ext}^I\}]$, is approximated by computationally advantageous expressions based on orbital-free DFT. For more information on sDFT, we refer the reader to several reviews.[34,35,46,47]

Particularly important in this work is the use of adaptive sDFT dynamics. That is, the AIMDs are run with a fluctuating number of subsystems. During the AIMD, when atoms of two fragments (molecules or ions) are closer than a predefined threshold distance (see covalent radii used for this purpose in the Supporting Information) the fragments are merged into a single subsystem. Conversely, when molecules belonging to the same subsystem move away, they are split into two separate subsystems. The specifics of the adaptive sDFT algorithms can be found elsewhere.[48] Examples of AIMD previously carried out with sDFT include several molecular condensed phase systems[49−51] and interfaces.[52]

In this work, all the simulation setups are composed of one metal ion atom (M^{2+}) and 117 H_2O water molecules. We added two chloride (Cl^-) counter-ions to the solvent phase to build a neutral system, in a cubic box of lattice vector a = 15.08 Å, corresponding to a molar concentration of 0.484 M which is in the same order of magnitude as the concentrations employed in the experiments considered in this work.

All the simulations have been carried out with the in-house code eDFTpy.[53] eDFTpy is an all-Python code implementing sDFT, where QEpy[54] is used as the DFT solver for the subsystems. QEpy is based on Quantum ESPRESSO 6.5.[55] The work and data are parallelized with mpi4py[56] with a method that reduces to a minimum gathering of large data sets described in detail in ref 52.

The revAPBEK[57] kinetic energy functional was employed as the nonadditive kinetic energy which is part of the nonadditive term of the energy functional in eq 2. We chose the DFT exchange−correlation functional PBE[58] for all subsystems and for the nonadditive part of the functional. For the metal-containing subsystem, we corrected PBE by the addition of the Hubbard U.[42−44] The U parameter was determined self-consistently (based on linear-response theory[42,44]) and independently for the octahedral and the square-planar geometries of each aqua ion (see Figures S1−S3). To avoid biasing toward octahedral or square-planar coordinations, we chose to use the average of the U parameters for the octahedral and square-planar geometries. The resulting U values are as follows: 6.79 eV for Ni, 0.78 eV for Pd, and 3.54 eV for Pt.

To model the electron−nuclear attraction potential, we used ultrasoft pseudopotentials from the GBRV library.[59] We opted for an energy cutoffs for the wave functions of each subsystem of 40 Ry, their density of 400 Ry and the total density (the sum of all subsystem densities) of 200 Ry. All input files and output files of our simulations are available on Zenodo.[60]

In line with established arguments from crystal field theory, the spin multiplicities were chosen to be singlet for low-spin square planer Pd^{2+} and Pt^{2+} and triplet for high-spin octahedral Ni^{2+}.[61] To validate the triplet spin multiplicity for Ni^{2+} in pure water, the solution-phase magnetic susceptibility was experimentally measured (μ_{eff} = 3.26 μ_B; see the Supporting Information for details).

AIMDs are run in the NVT ensemble (T = 300 K) for a total simulation time of 41, 30, 51, and 40 ps for $Ni^{2+}_{(aq)}$ in H_2O, $Ni^{2+}_{(aq)}$ in D_2O, $Pd^{2+}_{(aq)}$, and $Pt^{2+}_{(aq)}$ in H_2O, respectively. The time step was chosen to be 0.7 and 1.0 fs for simulations involving H_2O and D_2O solvents, respectively. The Berendsen thermostat with a temperature coupling parameter of 0.2 ps[62] was used. Optimization of the cluster structures is performed at the ωB97XD/def2-TZVP level with Gaussian 16 (Rev A.03).[63] Grimme's D3 dispersion corrections are employed for structure optimization.[64−67]

The EXAFS spectrum of $Pd^{2+}_{(aq)}$ was computed using FEFF8-lite.[68,69] The calculation employed an ensemble of 11,028 frames derived from the sDFT AIMD trajectory. The analysis incorporated multiple scattering effects, considering up to four-legged paths. Water molecules with Pd^{2+}−O distances less than 6 Å were included in the model structures.

TRAVIS has been used to compute radial, angular, and composite distribution functions (R/A/CDFs) and structure factors.[70] HB analyses were carried out with the MDAnalysis package (Version: 2.4.3).[71,72] Visual molecular dynamics (a.k.a., VMD)[73] and CYLview20[74] were used for displaying molecular structures.

Analysis of Available Experiments. An important result of this work is the interpretation of currently available experiments that probe the structure of the hydration shells around the metal ions. As mentioned before, experiments deliver global structure factors, and it is up to other means (simulations in this work) to dissect the global structure factors into partial, metal−oxygen, and metal−hydrogen structure factors that deliver the most relevant and useful structural information. We will see that even for the most established system, $Ni^{2+}_{(aq)}$, the experimental results (in particular for the metal−H_2O tilt angle) are contextualized and clarified by our simulations.

A summary of key structural descriptors can be found in Table 1. They include the metal−oxygen most probable distance ($R_{M^{2+}-O}$); the average and most probable metal−water tilt angle, θ, defined as the angle between metal−oxygen axis and the plane of the water molecule defined by the vector sum of the two OH bond vectors; and the coordination number of ligated oxygens to the metal center, CN_O. Let us now describe how each of the structure descriptors as extracted from the simulation compares against the experimental estimates for each of the three metal elements. The distributions of tilt angles, θ, for $Ni^{2+}_{(aq)}$, $Pd^{2+}_{(aq)}$, and $Pt^{2+}_{(aq)}$ are also provided in Figure S5.

In Figure 1, we present structure factors, partial Ni-D_2O and Ni-H_2O RDFs derived from the AIMD simulations based on sDFT against neutron diffraction (panels a−c) and X-Ray diffraction (panel d) experimental results. The sDFT structure factors and RDFs are obtained as follows. Due to the different relative concentration for different atoms and their varying scattering lengths, the total RDF of Ni with all other atoms in the system, $G_{Ni}(r)$, is formally expressed as the weighted summation of individual RDFs as[6,78]

https://doi.org/10.1021/acs.jpclett.4c00464
J. Phys. Chem. Lett. 2024, 15, 5517−5528

Table 1. Summary of Key Structural Descriptors for Group 10 Aqua Ions[a]

System	Properties	This work	Experiment
Ni^{2+}	$R_{Ni^{2+}-O}$	2.10 Å	2.072 ± 0.003 Å,[5] 2.07 ± 0.02 Å,[6] 2.05 Å[21], 2.06 ± 0.01 Å,[75] 2.069 ± 0.001 Å[76]
	θ (deg)	42.73° (50.70°)	42° ± 8°,[6] 40° ± 10°[77]
	CN_O	6	5.8 ± 0.2[6]
Pd^{2+}	$R_{Pd^{2+}-O}$	2.05 Å	2.04 Å[13]
	θ (deg)	52.67° (54.30°)	–
	CN_O	4	4[28]
Pt^{2+}	$R_{Pt^{2+}-O}$	2.04 Å	2.01 ± 0.01 Å,[28] 2.02 ± 0.02 Å[29]
	θ (deg)	50.23° (53.70°)	–
	CN_O	4	4[28,29]

[a]CN_O is the coordination number of O atoms around the metal center; θ is the tilt angle between the M−O axis and the plane of the same water molecule. Finally, $R_{M^{2+}-O}$ is the most probable metal−oxygen distance in the first hydration shell. The descriptors are extracted from our AIMD simulations, and experimental measurements with estimated errors. The column "This work" reports the average values of the metal−H_2O tilt angles, θ, directly from the simulations (accounting for thermal broadening). The most probable θ value is given in parentheses. The experimental estimate for Ni−H_2O θ is derived from peak metal−oxygen distances and assume an O−D bond length of 0.98 Å and a D−O−D angle of 105°.

$$G_{Ni}(r) = A[g_{Ni-O}(r) - 1] + B[g_{Ni-D}(r) - 1] + C[g_{Ni-Cl}(r) - 1] + D[g_{Ni-Ni}(r) - 1] \quad (3)$$

The constants $A = 0.64 \times 10^{-2}$ and $B = 1.46 \times 10^{-2}$ are taken from ref 6, which involved a 1.46 molal (about 1.4 M) $NiCl_2$ solution in D_2O. We stress that even though our simulations consider 0.484 M solutions, the ratio of the A and B constants for the experimental concentration and the one considered in our simulations are essentially the same.

The structure factors (panels a and b of Figure 1) provide the most straightforward comparison of our simulations with the raw experimental data. It is clear that the sDFT results lie within 1σ of the experimental fit almost everywhere. We note that the low-Q region of the structure factor cannot be reproduced by simulations for two reasons (also mentioned in the description of Figure 2). Namely, the finite-size effect in the simulations and a potential residual inelastic scattering from the experiment. As mentioned before, the reason for the high level of noise in the experimental data is the fact that these structure factors are found by taking the difference between the structure factors of two $NiCl_2$ solutions. As the neutron scattering is dominated by the scattering of the water solvent, the difference signal is about 0.5−3% of the total scattering intensity. Fourier transform of these structure factors generates the $G_{Ni}(r)$ in Figure 1c. The uncertainty given as gray shade was estimated in the Supporting Information as the difference between two RDFs produced by two independent experiments reported in ref 79. The comparison shows that our sDFT simulations accurately predict the location of the first two peaks of $G_{Ni}(r)$ (2.10 Å and 2.67 Å), which correspond to Ni−O and Ni−D distances, compared with experimental peaks, which are located at 2.06 Å and 2.65 Å. The sDFT prediction for the Ni−O peak also agrees with other experimental results, i.e., 2.07 Å reported in previous neutron diffraction (1.4 M $NiCl_2$ solution[6]), and XRD (2.951 M $NiCl_2$ solution[76]). sDFT also reproduced the location (4.01 Å) and width of the second hydration shell as seen in the comparison to X-Ray data in Figure 1d as well as with EXAFS (4.00 Å from ref 5).

An important aspect of our work is the analysis of the metal−water tilt angle, θ, described before. The tilt angle is a property that fluctuates greatly due to thermal effects. In $Ni^{2+}_{(aq)}$, the distribution of θ is very broad and nonsymmetric compared to Pd and Pt aqua ions. The average, mean value of θ is 42.73° and differs greatly from its most probable value (i.e., the peak of the distribution) of 50.7°. The experiment values of 42° and 40° were derived based on the assumptions that the D−O−D angle and the O−D distance, are 105° and 0.98 Å, respectively. The significant asymmetry of the θ distribution is evident in our simulations and has also been reported, although to a lesser degree, in previous AIMD

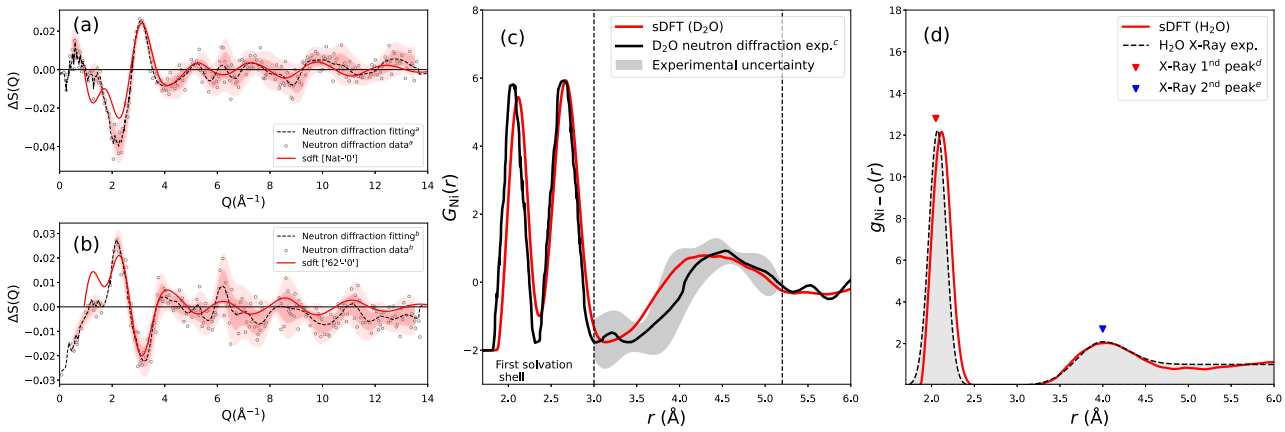

Figure 1. (a and b) Structure factor difference of a 1.43 molal solution of $NiCl_2$ between naturally occurring Ni ("Nat") (a) and ^{62}Ni ("62") (b) with $NiCl_2$ solution that is a mixture of natural and "62" and has nearly zero neutron scattering length (called "0"). Circles are the raw experimental data; dashed black line is the experimental fit of the data, and the red shadings are 1σ (dark red shade) and 2σ (light red shade). sDFT results are the red solid lines. (c and d) Radial distribution functions (RDFs) for Ni^{2+} aqua ion from our simulation (red lines), experiment (black lines), and experimental uncertainty range (gray shade). (c) RDF of all atom pairs containing Ni, $G_{Ni}(r)$. (d) Partial Ni−O RDF, $g_{Ni-O}(r)$. X-ray diffraction measurements locate the first hydration shell peak at 2.07 Å and the second hydration shell peak at 4.00 Å. For ease of comparison, the peaks are represented by Gaussian functions of width taken from the experimental measurements. [[a]From Figure 4.17(a) in ref 79. [b]From Figure 4.17(b) in ref 79. [c]From ref 6. [d]From refs 5, 76. [e]From ref 5.]

https://doi.org/10.1021/acs.jpclett.4c00464
J. Phys. Chem. Lett. 2024, 15, 5517−5528

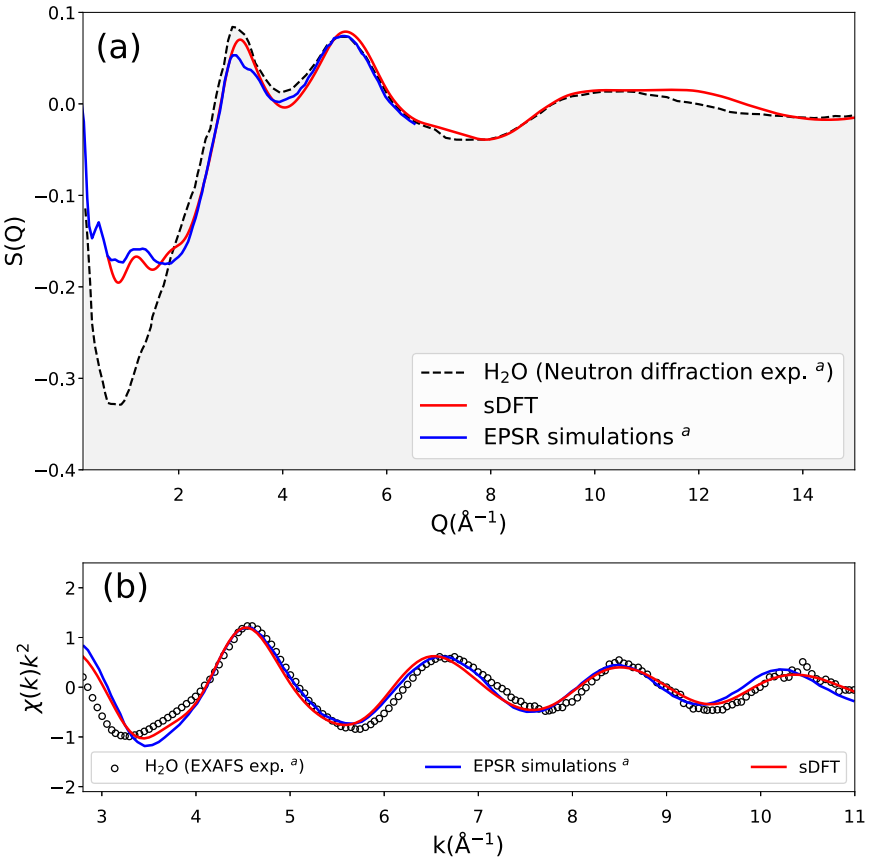

Figure 2. (a) Structure factor associated to all atom pairs for $Pd^{2+}_{(aq)}$. Neutron diffraction experiment (shaded, black dashed line), sDFT simulation (red line), reverse Monte Carlo (EPSR) simulations (blue line). [^{a}Fom ref 13.] (b) Pd K-edge k^2-weighed EXAFS of $Pd^{2+}_{(aq)}$. EXAFS experiment (circles), sDFT simulation (red line), and reverse Monte Carlo (EPSR) simulation (blue line).

simulations of Ni aqua ion based on the semilocal exchange−correlation functional PBE[8] where the average and peak values were found to be 43.5° and 47°, respectively.

Next, we compare the neutron diffraction structure factor $S(Q)$ of $Pd^{2+}_{(aq)}$. Figure 2 displays the structure factor from neutron scattering experiments as well as calculated ones from our simulations (sDFT) and the EPSR simulations from ref 13. We recall that, similar to eq 3, the total $S(Q)$ is expressed as a linear combination of the partial structure factors of different interaction pairs between atom α and β. $S_{\alpha\beta}(Q)$, given by

$$S(Q) = N \sum_{\alpha,\beta=1}^{n} c_\alpha c_\beta b_\alpha b_\beta S_{\alpha\beta}(Q) \tag{4}$$

where the c_α is the molar concentration of atom α, b_β represents the neutron scattering length of atom β, and N is a normalization constant.

An analysis of eq 4 shows that the total structure factor is only weakly sensitive to the fine structure of the partial structure factor $S_{Pd-O}(Q)$ due to the low concentration of Pd^{2+}−O atom pairs in comparison to the overwhelmingly larger O−O atom pair concentration from the solvent. For the structures considered in our simulations, the ratio is of 1 Pd^{2+}−O pair for every 200 O−O pairs. This observation necessarily weakens the results from ref 13 (indicated by EPSR, hereafter) which computes $S(Q)$ from molecular dynamics simulations on force fields that are adjusted to find a best fit to the experimental structure factor. Such a fit predominantly optimizes the partial structure factors involving only H and O atoms.

Figure 2a shows that the $S(Q)$ derived by our sDFT simulations (neutron scattering lengths were taken from the NIST database[80]) is also very close to the experimental $S(Q)$ for Q larger than 2 Å^{-1}. In fact, the overall structure factor and in particular the first peak near 3 Å^{-1} is better described by sDFT compared to the EPSR simulations. Yet, due to the limited size of the simulation unit cells, both sDFT and EPSR are unable to reproduce the $S(Q)$ in the low-Q limit. The inability to compare the low-Q parts of $S(Q)$ could be ascribed to the well-known finite-size effects[81] and, in this case, also to residual inelastic scattering. This does not affect our predictions or results in any way.

Figure 2b shows a comparison among experimental EXAFS spectra and two simulated counterparts (EPSR and sDFT). The experimental and EPSR data sets were extracted and digitized from ref 13. Notably, a favorable alignment between the sDFT-simulated spectra and the experimental data is also observed. Because of the elemental specificity inherent in EXAFS, it is a highly sensitive technique exclusively targeting the local environment of Pd^{2+}. The agreement also stipulated that our sDFT simulation is capable of accurately representing the solvation shells of Pd^{2+}. Figure S7 collects a comparison of EXAFS spectra collected by two separate experiments. The EXAFS spectrum from ref 14 is somewhat different from the one from ref 13 likely because of the employment of different techniques for normalization and subtraction of the baseline in the spectrum. However, the two EXAFS experimental spectra

https://doi.org/10.1021/acs.jpclett.4c00464
J. Phys. Chem. Lett. 2024, 15, 5517−5528

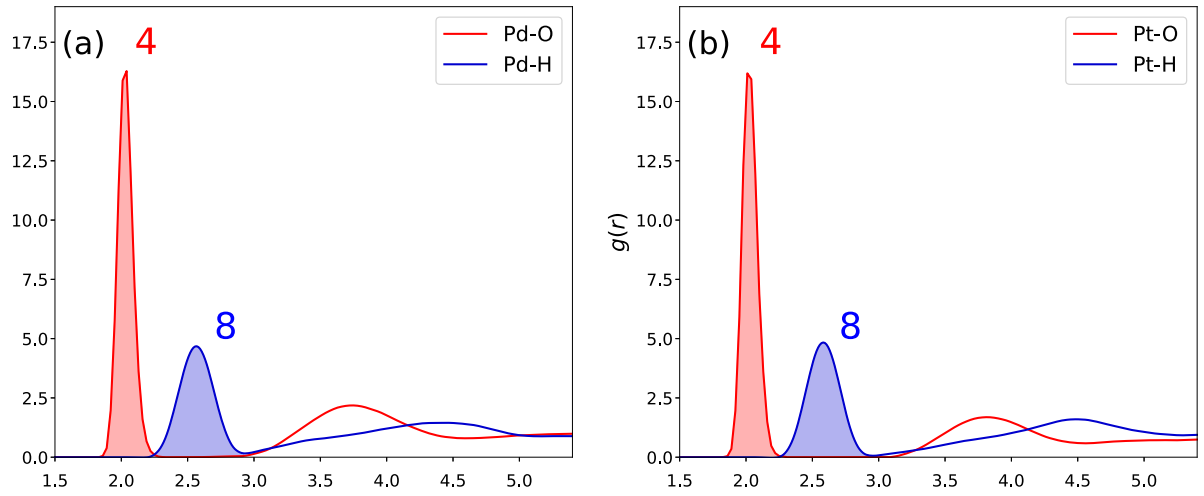

Figure 3. Metal−oxygen (red) and metal−hydrogen (blue) RDFs: (a) Pd^{2+} and (b) Pt^{2+}. The coordination numbers for H and O atoms are printed next to the corresponding peaks.

share similar features which are also reproduced in the simulations.

Looking back at Table 1, we see that the most probable Pd^{2+}−O distance is well reproduced by our simulations, which underestimates the experimental estimation by barely 0.01 Å.

For $Pt^{2+}_{(aq)}$, we only consider the results of the experimental measurements summarized in Table 1 which were taken from refs 28 and 29. The sDFT simulation results show a slight overestimation of about 0.03−0.04 Å for the Pt^{2+}−O most probable distance. Interestingly, the structural descriptors predicted by our simulations do not clearly distinguish the hydration of $Pt^{2+}_{(aq)}$ from $Pd^{2+}_{(aq)}$. However, we will see that the predicted dynamic behavior of the hydration shells of these two ions is noticeably different.

Hydration Shell Structure. The hydration shell structures predicted by our simulations for $Pd^{2+}_{(aq)}$ and $Pt^{2+}_{(aq)}$ are compared in Figure 3, where the partial M−O and M−H RDFs are compared side by side. In Figure 4 we report the ADFs for the metal−oxygen bonds of the first hydration shell.

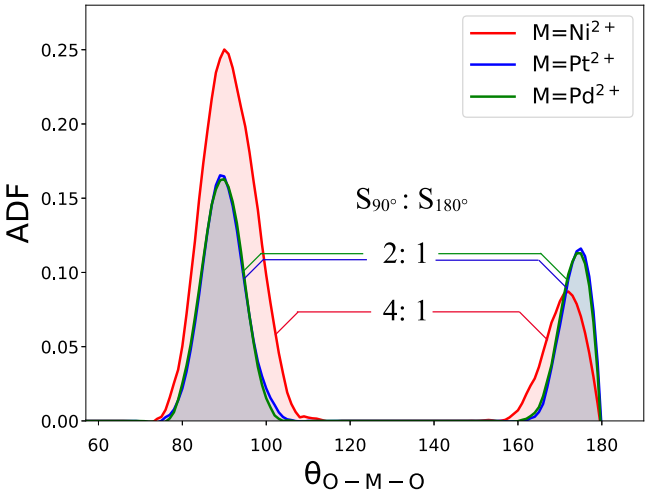

Figure 4. ADFs for the intramolecular θ_{O-M-O} angle of the three group 10 aqua ions. $S_{90°}$ and $S_{180°}$ are the integral areas of first and second peaks, respectively. The ratios of $S_{90°}$:$S_{180°}$ are printed in the figure.

The M^{2+}−O and M^{2+}−H RDFs of both $Pd^{2+}_{(aq)}$ and $Pt^{2+}_{(aq)}$ are quite similar to each other. Specifically, the first peaks of the M^{2+}−O RDFs for both ions are located at around 2.05 Å, and their integrals equal 4, which indicates coordination by 4 water molecules. The first hydration peaks for hydrogen atoms are broader than those for oxygen atoms and located around 2.56 Å for both $Pd^{2+}_{(aq)}$ and $Pt^{2+}_{(aq)}$.

The second hydration shells for both Pd^{2+}−O and Pt^{2+}−O start before 3.00 Å, which is a shorter metal−oxygen distance than for Ni^{2+} (with a second hydration peak beginning at 3.30 Å). We notice that the Pd^{2+}−O peak associated with the second hydration shell is somewhat broader than that of Pt^{2+}−O. However, contrary to the EPSR[13] and the force field-based simulations,[11] a sharp peak between the first and second shells for Pd^{2+} does not appear in our results. A Car−Parrinello Molecular Dynamics (CPMD) simulation of this system[17] also did not find the sharp peak between the first and second shells. The comparison between RDFs from the several simulations available in the literature and the present work are presented in Figures S8−S10.

The analysis of O−M^{2+}−O ADFs provides further insights into the structure of the aqua ions (see Figure 4). In the case of Ni^{2+}, the ADF peaks are located between 76°−107° and 160°−180°, with the maxima at 90° and 171°, respectively. The ADF shapes of O−Pd^{2+}−O and O−Pt^{2+}−O are similar to each other, but different from that of O−Ni^{2+}−O. Both $Pd^{2+}_{(aq)}$ and $Pt^{2+}_{(aq)}$ aqua ions have two peaks at ranges of 77°−102° and 160°−180°, with maxima at 90° and 175°. The integral areas between the first and second peaks are 4:1, 2:1, and 2:1, respectively, clearly indicating that the water coordination of $Ni^{2+}_{(aq)}$ is octahedral, while that of $Pd^{2+}_{(aq)}$ and $Pt^{2+}_{(aq)}$ aqua ions is square-planar.

To shed light on the predicted structure of the second-shell hydration in the three aqua ions considered, we present in Figure 5 the combined radial-angular distribution function (CDF) for these systems. Inspection of the top panels of the figure shows that for Ni^{2+}, no significant axial second hydration shell is present. This is a consequence of the fact that aqua Ni has a bound water in the axial position at about 2 Å distance. This generates a vacuum of water molecules (oxygen atoms) until about 4.5 Å. For Pd and Pt aqua ions the CDF shows a different picture. The axial solvation is occupied by water. These concentrate at 3.5 Å for Pd and at 4.5 Å for Pt. The Pd

https://doi.org/10.1021/acs.jpclett.4c00464
J. Phys. Chem. Lett. 2024, 15, 5517−5528

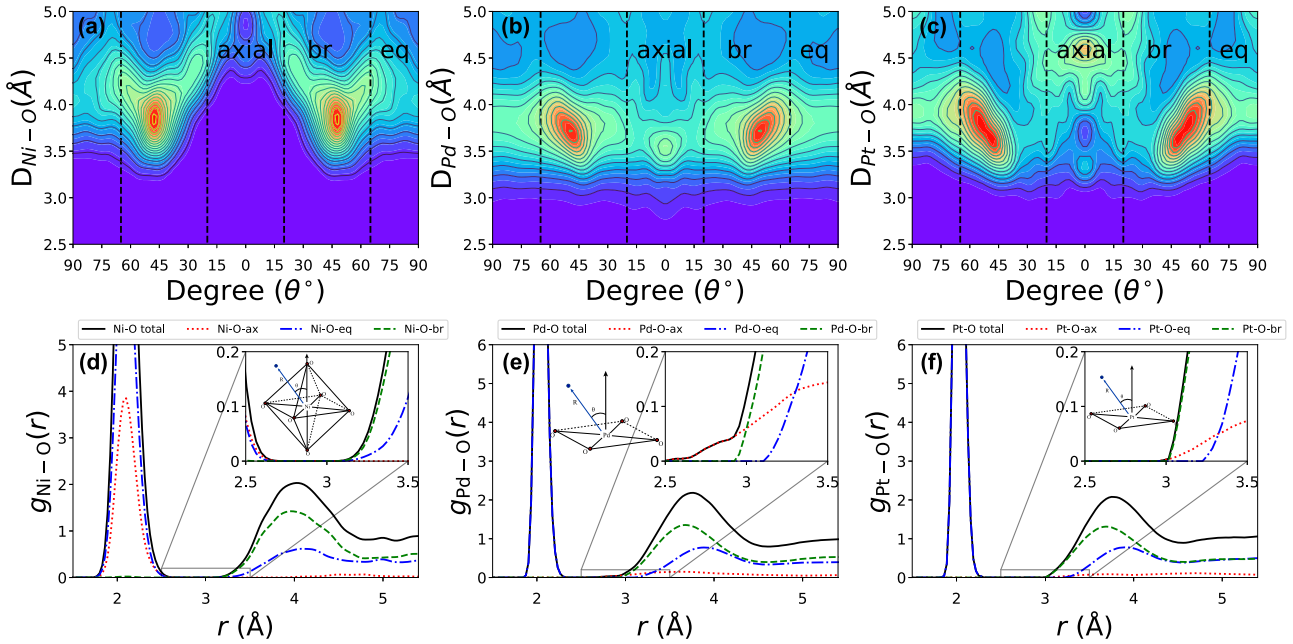

Figure 5. (a–c) Combined radial distribution function for the metal–oxygen atom pairs distance and azimuthal angle with normal to the aqua ion plane. (d–f) Decompostion of $g_{Pd-O}(r)$ into equatorial (eq), bridge (br), and axial (axial) regions. A visual of the three regions is provided in Figure S11.

aqua ion is particularly interesting as it shows bridge and axial shells blending into a single feature with three maxima (one for each bridge region and one for the axial position). The panels in the lower part of the figure simply trace the angles in between the boundaries indicated in the upper panels; also provided in the inset is a zoomed-in view of the region of metal–oxygen distances between 2.5 and 3.5 Å. While for Pd a nonzero RDF for axial waters is already detectable right after 2.5 Å, the feature does not amount to a sharp isolated peak; instead, it develops into a broad peak centered at ∼3.5 Å.

Hydration Shell Dynamics. The hydration shell structure analysis carried out thus far only provides information about the thermal average structure. In reality, thermal fluctuations occur in the structure that make it depart from the average. These fluctuations are captured by our simulations and are the subject of the following discussion. Water dynamics is closely related to the ability of water to self-diffuse. Even though AIMD simulations with semilocal DFT exchange–correlation functionals were shown to severely underestimate the self-diffusion of water,[82,83] sDFT with semilocal nonadditive functionals was shown to provide a perfect balance of nonadditive exchange–correlation and nonadditive kinetic energy allowing it to model liquid water in a quantitatively correct way.[39] sDFT's value for the water self-diffusion is 3.0 ± 0.4 × 10^{-5} cm^2 s^{-1} against an experimental value of 2.34 in the same units.

In order to characterize the mobility of water in the first and second hydration shells, the time evolution of the shortest 18 M^{2+}–O distances are evaluated from the simulations' trajectories and shown in Figure 6. The clear boundary between the two hydration shells further indicates that there is no intershell water exchange in the time scale of our simulations (tens of ps). This is consistent with the analysis of the RDFs presented previously and with the known water exchange rates for these complexes.[9]

The Ni^{2+}–O distance of the first hydration shell has a larger fluctuation than the Pd^{2+}–O and Pt^{2+}–O distances. The Ni^{2+}–O bond distance can fluctuate to 2.6 Å (see Figure 6 at 4.0 ps for Ni), which deviates substantially from the average distance of 2.14 Å. In contrast, the four coordinated waters in Pd^{2+} and Pt^{2+} are tightly bound to their metal centers.

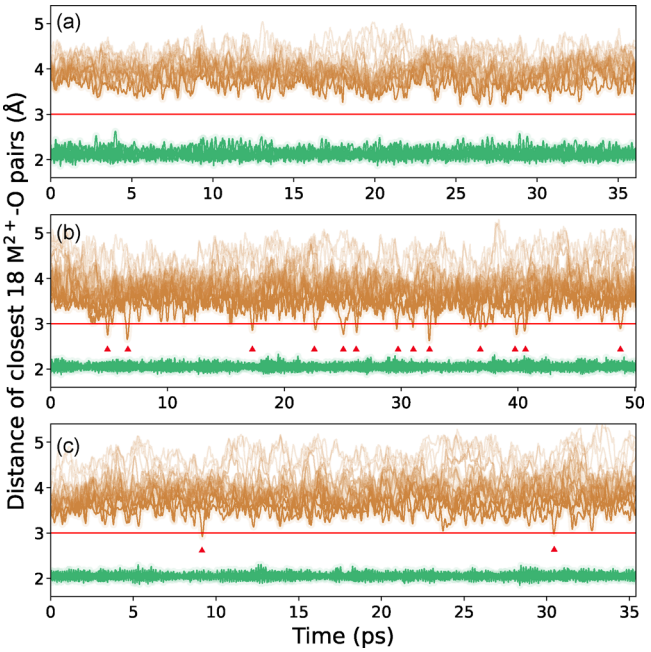

Figure 6. Time evolution of the 18 shortest metal–oxygen distances for (a) Ni^{2+}, (b) Pd^{2+}, and (c) Pt^{2+} aqua ions. The first hydration shell is highlighted in green. The 3 Å threshold is indicated by the horizontal lines. Triangles label second shell water entry events into the region where the M^{2+}–O distance is <3 Å. Lines are set to become more transparent as the water molecules are located farther from the metal center.

The mobility of the second hydration shell differs for the three aqua ions. For Ni^{2+}, due to sterics provided by the 6

https://doi.org/10.1021/acs.jpclett.4c00464
J. Phys. Chem. Lett. 2024, 15, 5517–5528

waters in the first hydration shell, the second shell is well separated at a distance of 3.3 Å from the metal center. In contrast, the second hydration shell in Pd^{2+} is softer, clearly displaying the short-lived and transitory nature of water molecule penetration in the intermediate region. The minimum Pd^{2+}−O distance is 2.63 Å at 33.4 ps. Conversely, the second hydration shell for Pt^{2+} is rigid in comparison to the $Pd^{2+}$with only one Pt^{2+}−O distance reaching a length less than 3.00 Å throughout the entire AIMD trajectory.

We provide a visual of the molecular-level structure for the mentioned hydration shell fluctuations in Figure 7. In the

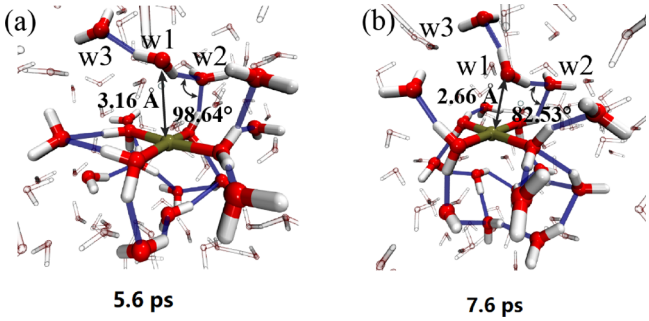

Figure 7. Two snapshots following a water molecule (w1) entering the intermediate region between the first and second hydration shells of Pd^{2+}. At 5.6 ps, panel a shows a defected HB network (there are fewer water molecules linked directly and indirecly to aqua ion above the aqua ion plane than below the plane). Panel b shows that the shortest Pd^{2+}−O distance of 2.66 Å is reached at 7.6 ps, where w1 enters the intermediate region between the first and second hydration shells. The HBs of molecules w1, w2, and w3 are represented by blue transparent bonds.

figure, the first hydration shell and second hydration shell water molecules connected directly and the nearest indirectly connected to the aqua ion via HBs are highlighted. We see in panel a of Figure 7 that at 7.3 ps there are less hydrogen bonded water molecules in the region above the $Pd^{2+}_{(aq)}$ plane (4 waters, w3 is not included) than in the region below the plane (7 waters). The water molecules below the $Pd^{2+}_{(aq)}$ aqua ion plane form an HB network. Conversely, another side above the plane shows an HB network defect. An important consequence of the HB defect is that the water molecule labeled as w1 in Figure 7 is less restrained by the HB network and could move toward the metal center, reaching the short distance of 2.66 Å as can be seen in the second snapshot in panel b of the figure. The short metal−water distance also results in a transient and twisted HB structure. The HB angle of water w2 (82.53°, see figure for details) is much smaller than for a typical HB (109.47° found in water ice). This process is also illustrated in the video whose link is provided in the Supporting Information.

However, such transient, defective HB network states are rare and a stable axial ligation of water on Pd^{2+} does not occur. In view of this analysis, we conclude that water molecules do not stably ligate axially in the Pd^{2+} aqua ion because they are "locked" in a stiff HB network that, at least at room temperature, is seldom disrupted.

The Hydrogen Bond "Dome" Concept. The previous considerations highlight that the Coulomb attraction between axial waters and bare Pd^{2+} or Pt^{2+} cations is contrasted by a resilient HB network. In order to describe the HB network in the axial region of the second hydration shell, we analyzed our trajectories using a loose definition of HB (oxygen donor−acceptor distance cutoff of 3.3 Å and a donor−hydrogen−acceptor angle greater than 145°). To avoid counting HBs from water in the equatorial region, we focused on the HBs forming above and below the square planar complex plane (selected by the angle between M^{2+}−O vector and aqua ion planes ranging from 15° to 90° on both sides of the plane of the metal complex). We further filtered the water molecules by their topology. That is, only water molecules that are either nearest neighbor of the metal center or H-bonded to a nearest neighbor molecule are included.

Figure 8 summarizes this analysis correlating the shortest metal−oxygen distance in the second hydration shell with the number of water molecules involved in the axial HB network. The data in Figure 8 has been filtered by a Viterbi algorithm with a two-state hidden Markov model to filter out noise from thermal fluctuations.[84]

The maximum number of axial H-bonded water molecules for $Pd^{2+}_{(aq)}$ and $Pt^{2+}_{(aq)}$ on either side of the plane (below or above the aqua ions plane) is 9. When the number of axial H-bonded waters on one side of the square plane is 3 or less, the HB network enters a defective, fluxional state. The axial HB network of $Pd^{2+}_{(aq)}$ is softer than that of $Pt^{2+}_{(aq)}$, as the number of axial H-bonded waters on one side for $Pd^{2+}_{(aq)}$ often falls below 3 to 1. A crucial observation is that the number of water molecules entering the axial region of $Pd^{2+}_{(aq)}$ is anticorrelated with the total number of axial H-bonded waters. Four events of water entering into the axial region of Pd(II) aqua ion (Pd−O distance less than 3 Å) are marked on Figure 8a. The four structures with shortest Pd−O distances are depicted in Figure 8c. In structures 1−3, the water molecules in the axial region of Pd^{2+} are located on the sides with fewer axial HB waters, resulting in a lack of HB constraints. Conversely, in structure 4, the closest water molecule is involved in a twisted HB. However, the presence of twisted HB structures in this case leads to an exclusion rather than stabilization effect on the water molecule, owing to the relaxation of tension in the HB structure.

Combined with the discussion of hydration shell dynamics, our results suggest that a defect in the HB network is a necessary condition for water molecules entering the axial region of $Pd^{2+}_{(aq)}$ and $Pt^{2+}_{(aq)}$ aqua ions. We conclude that the constraints imposed by the axial HB network play a dominant role in determining the hydration shell dynamics.

To provide a visual for the axial H-bonded water molecules, we selected one AIMD snapshot of $Pd^{2+}_{(aq)}$ at 11.5 ps (selected because of the large number (12) of axial HB waters), carved a cluster containing the metal center and 20 water molecules, and performed geometry relaxation in vacuum. The optimized structure of a $Pd^{2+}_{(aq)}$ cluster was then utilized as an initial guess for the optimization of $Pt^{2+}_{(aq)}$. The structure resulting after relaxation is depicted in Figure 9. The absence of the condensed phase environment and the fact that geometry relaxations deliver so-called zero-Kelvin structures; the resulting hydration shell is more compact compared to the average one obtained from the AIMD simulations.

Figure 9 clearly shows that the HB network has a tendency to arrange in a dome shape. The number of H-bonded dome waters in the figure for both $Pd^{2+}_{(aq)}$ and $Pt^{2+}_{(aq)}$ aqua ions is 10, which is consistent with the AIMD results. This additional analysis reveals no water molecules in close proximity to the metal cation centers. The minimum Pd^{2+}−O and Pt^{2+}−O distances are 3.22 Å and 3.39 Å, respectively. Even though

https://doi.org/10.1021/acs.jpclett.4c00464
J. Phys. Chem. Lett. 2024, 15, 5517−5528

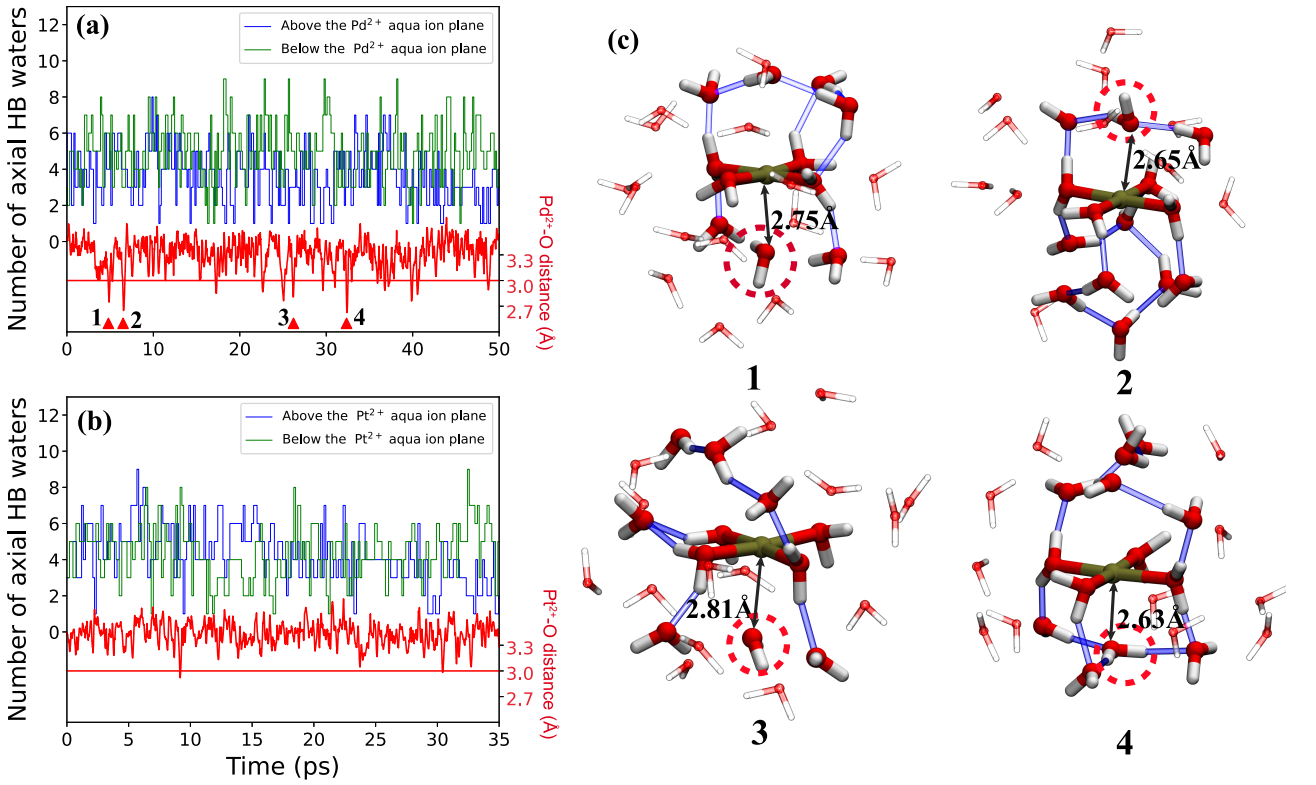

Figure 8. Blue and green lines: The time evolution of the number of water molecules in the axial HB network above and below the aqua ions plane, respectively (see text for details). Red line: Shortest metal−oxygen distance from the second hydration shell. Four water entering into the axial region events are selected to illustrate the relationship between water penetration and nearby HB networks. The defective axial HB network is a necessary condition for the penetration of second-shell waters in the intermediate region between the hydration shells.

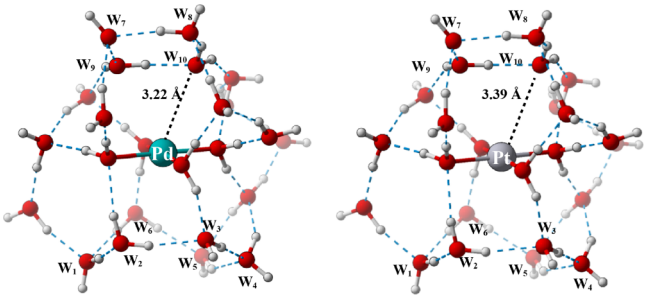

Figure 9. Optimized $Pd^{2+}_{(aq)}$ and $Pt^{2+}_{(aq)}$ clusters. The shortest metal−oxygen distance is 3.22 Å and 3.39 Å for Pd and Pt, respectively. The HBs are indicated by blue dashed lines. The ten dome waters are labeled W_1−W_{10}. Of these, six waters located below the aqua-ion planes are arranged in a six-membered ring, while the remaining four waters located above the aqua-ion plane form a four-membered ring.

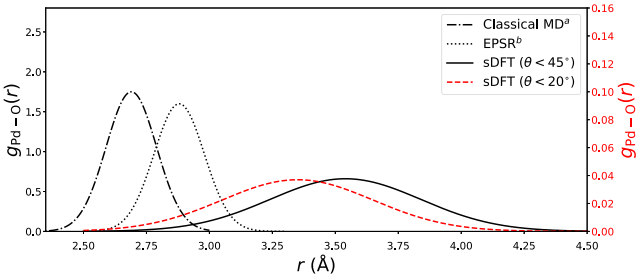

Figure 10. Contribution of axial waters to the metal−oxygen RDF taken from [a]ref 11 (black dash-dotted line), [b]ref 13 (black dotted line), and our sDFT AIMD simulations where the axial region is defined by azimuthal angle up to 45° (black solid line) and 20° (red dashed line). The data from refs 11 and 13 were extracted by fitting the mesoshell sharp peaks by Gaussian functions. The sDFT data were fitted with a Gaussian function from the decomposed $g_{Pd-O}(r)$ of the axial region presented in Figure 5.

these distances are still larger than those predicted by simulations featuring the mesoshell of axial water,[11,13] Figure 9 provides a picture similar to Figure 5 of ref 11, albeit featuring a further away and broader axial hydration shell. Particularly telling is the information available in Figure 10, as we compare the RDFs of the axial Pd−O pairs from sevral works. The Pd−O axial hydration predicted by sDFT features broader RDF peaks. Specifically, when the waters within 20° of azimuthal angle are considered, the peak of the axial shell is at 3.35 Å. The peak shifts to 3.54 Å when the azimuthal angle boundary is increased to 45°, likely because, according to Figure 5, water molecules in the bridge region are also partially included, thus shifting the peak.

In summary, sDFT AIMD simulations predict that water is dynamically diffusive toward the Pd metal center, influenced by the balance between hydrogen bond networks and Coulomb attraction from the metal centers.

In conclusion, in this work we employ accurate yet computationally amenable ab initio molecular dynamics simulations based on subsystem DFT to explore the hydration shell structure and dynamics of group 10 aqua ions ($Ni^{2+}_{(aq)}$, $Pd^{2+}_{(aq)}$, and $Pt^{2+}_{(aq)}$). To our knowledge, this work provides the most accurate description of these hydrated ions to date. Our simulations are accurate, as they closely match the available experimental data for the three ions.

https://doi.org/10.1021/acs.jpclett.4c00464
J. Phys. Chem. Lett. 2024, 15, 5517−5528

An important focus of this work is the structure and dynamics of the second hydration shell (i.e., the water molecules beyond the ones directly coordinated to the metal center). Our simulations and our analysis of the available experimental data through the lenses of our ab initio dynamics simulations shed light particularly on axial hydration. To date, axial hydration of Pd is characterized by the "mesoshell" concept.[13,14] The mesoshell is identified by a clear, sharp peak in the partial Pd−O RDF sitting between the first and the second solvation shell. Our analysis refines this view finding that the sharp mesoshell is rather a broader feature with an onset at 2.5 Å and extending up to 4.3 Å, approximately. Our analysis goes beyond structural considerations and ventures into the characterization of the dynamics of the hydration shells. By monitoring the distances ($R_{M^{2+}-O}$) between the cation center M^{2+} and the nearby O atoms, we found that the water molecules rarely visit the axial region ($R_{Pd^{2+}-O} < 3$ Å). By visualizing the AIMD trajectories, we found that the waters in the second hydration shell are bound by a resilient HB network which counteracts the attraction to the cation center.

Optimized snapshots from the AIMD show that the HB network in the axial region of Pd and Pt forms a protective "dome" on both sides of the $Pd^{2+}_{(aq)}$ and $Pt^{2+}_{(aq)}$ aqua ion planes. The domes counteract water penetration from the axial directions. We ascribe to the existence of the domes the fact that our interpretation of the experimental data is more consistent with a broad axial solvation shell rather than a mesoshell for $Pd^{2+}_{(aq)}$.

The interpretation of condensed-phase chemical reactions involving Pd^{2+} in water must consider the influence of the "dome" structure. This dome, a robust hydrogen bonding network, needs to be disrupted before any ligand can coordinate with the metal ion. Consequently, mechanistic analyses of catalytic reactions in aqueous environments should account for the dome's potential effects.

■ ASSOCIATED CONTENT

Supporting Information

The Supporting Information is available free of charge at https://pubs.acs.org/doi/10.1021/acs.jpclett.4c00464.

Determination of Hubbard U; determination of experimental uncertainty of $G_{Ni}(r)$ including discussion (Figure S4); tilt angle distribution discussion (Figure S5); RDF comparison of Ni^{2+} in H_2O and D_2O solvents (Figure S6); comparison of EXAFS (Figure S7); comparison of RDFs (Figures S8−S10); and definition of different regions of second solvation shell (Figure S11) (PDF)

■ AUTHOR INFORMATION

Corresponding Authors

Xin Chen − *Department of Chemistry, Rutgers University, Newark, New Jersey 07102, United States; Department of Physics, Rutgers University, Newark, New Jersey 07102, United States;* orcid.org/0000-0002-5227-1334; Email: chen.xin@rutgers.edu

Xuecheng Shao − *Department of Chemistry, Rutgers University, Newark, New Jersey 07102, United States;* orcid.org/0000-0003-2215-0926; Email: xuecheng.shao@rutgers.edu

Michele Pavanello − *Department of Chemistry, Rutgers University, Newark, New Jersey 07102, United States; Department of Physics, Rutgers University, Newark, New Jersey 07102, United States;* orcid.org/0000-0001-8294-7481; Email: m.pavanello@rutgers.edu

Authors

Andres Cifuentes-Lopez − *Department of Chemistry, Rutgers University, Newark, New Jersey 07102, United States;* orcid.org/0000-0002-7861-0111

Lirong Lin − *Department of Chemistry, Rutgers University, Newark, New Jersey 07102, United States*

Demyan Prokopchuk − *Department of Chemistry, Rutgers University, Newark, New Jersey 07102, United States;* orcid.org/0000-0002-6352-3509

Complete contact information is available at: https://pubs.acs.org/10.1021/acs.jpclett.4c00464

Author Contributions

¶X.C. and A.C.-L. contributed equally to the work.

Notes

The authors declare no competing financial interest.

■ ACKNOWLEDGMENTS

This material is based upon work supported by the National Science Foundation under Grant Nos. CHE-2154760 and OAC-1931473, and Petroleum Research Fund Grant No. 62555-ND6. L.L. and D.P. acknowledge Petroleum Research Fund Grant No. 66371-ND3.

■ REFERENCES

(1) Nakayama, M.; Suzuki, K.; Fujii, K. Single-ion Catalyst of Ni^{2+} Anchored in the Interlayer Space of Layered MnO_2 for Electro-oxidation of Ethanol in Alkaline Electrolyte. *Electrochem. Commun.* **2019**, *105*, 106492.

(2) Vicente, J.; Arcas, A. Aqua Palladium Complexes: Synthesis, Properties and Applications. *Coord. Chem. Rev.* **2005**, *249*, 1135−1154.

(3) Zhou, F.; Hearne, Z.; Li, C.-J. Water—the Greenest Solvent Overall. *Current Opinion in Green and Sustainable Chemistry* **2019**, *18*, 118−123. Special Issue on Africa − Green solvents.

(4) Leininger, S.; Olenyuk, B.; Stang, P. J. Self-Assembly of Discrete Cyclic Nanostructures Mediated by Transition Metals. *Chem. Rev.* **2000**, *100*, 853−908. PMID: 11749254.

(5) D'Angelo, P.; Barone, V.; Chillemi, G.; Sanna, N.; Meyer-Klaucke, W.; Pavel, N. V. Hydrogen and Higher Shell Contributions in Zn^{2+}, Ni^{2+}, and Co^{2+} Aqueous Solutions: An X-ray Absorption Fine Structure and Molecular Dynamics Study. *J. Am. Chem. Soc.* **2002**, *124*, 1958−1967.

(6) Neilson, G. W.; Enderby, J. E. The Hydration of Ni^{2+} in Aqueous Solutions. *J. Phys. C: Solid State Phys.* **1978**, *11*, L625.

(7) Varadwaj, P. R.; Cukrowski, I.; Marques, H. M. DFT-UX3LYP Studies on the Coordination Chemistry of Ni^{2+}. Part 1: Six Coordinate $[Ni(NH_3)_n(H_2O)_{6-n}]^{2+}$ Complexes. *J. Phys. Chem. A* **2008**, *112*, 10657−10666.

(8) Mareš, J.; Liimatainen, H.; Laasonen, K.; Vaara, J. Solvation Structure and Dynamics of Ni^{2+}(aq) from First Principles. *J. Chem. Theory Comput.* **2011**, *7*, 2937−2946. PMID: 26605483.

(9) Rotzinger, F. P. Mechanism of Water Exchange for the Di- And Trivalent Metal Hexaaqua Ions of the First Transition Series. *J. Am. Chem. Soc.* **1997**, *119*, 5230−5238.

(10) Eigen, M. Fast Elementary Steps in Chemical Reaction Mechanisms. *Pure Appl. Chem.* **1963**, *6*, 97−116.

(11) Martínez, J. M.; Torrico, F.; Pappalardo, R. R.; Sanchez Marcos, E. Understanding the Hydration Structure of Square-planar Aquaions: the $[Pd(H_2O)_4]^{2+}$ Case. *J. Phys. Chem. B* **2004**, *108*, 15851−15855.

(12) Torrico, F.; Pappalardo, R. R.; Marcos, E. S.; Martínez, J. M. Hydration Structure and Dynamic Properties of the Square Planar Pt

(II) Aquaion Compared to the Pd (II) Case. *Theor. Chem. Acc.* **2006**, *115*, 196−203.
(13) Bowron, D. T.; Beret, E. C.; Martin-Zamora, E.; Soper, A. K.; Sánchez Marcos, E. Axial Structure of the Pd (II) Aqua Ion in Solution. *J. Am. Chem. Soc.* **2012**, *134*, 962−967.
(14) Purans, J.; Fourest, B.; Cannes, C.; Sladkov, V.; David, F.; Venault, L.; Lecomte, M. Structural Investigation of Pd(II) in Concentrated Nitric and Perchloric Acid Solutions by XAFS. *J. Phys.Chem. B* **2005**, *109*, 11074−11082. PMID: 16852349.
(15) Shah, S. A. A.; Hofer, T. S.; Fatmi, M. Q.; Randolf, B. R.; Rode, B. M. A QM/MM MD Simulation Study of Hydrated Pd^{2+}. *Chem. Phys. Lett.* **2006**, *426*, 301−305.
(16) Hofer, T. S.; Randolf, B. R.; Adnan Ali Shah, S.; Rode, B. M.; Persson, I. Structure and Dynamics of the Hydrated Palladium(II) Ion in Aqueous Solution a QMCF MD Simulation and EXAFS Spectroscopic Study. *Chem. Phys. Lett.* **2007**, *445*, 193−197.
(17) Beret, E. C.; Martínez, J. M.; Pappalardo, R. R.; Marcos, E. S.; Doltsinis, N. L.; Marx, D. Explaining Asymmetric Solvation of Pt(II) Versus Pd(II) in Aqueous Solution Revealed by Ab Initio Molecular Dynamics Simulations. *J. Chem. Theory Comput.* **2008**, *4*, 2108−2121.
(18) Rizzato, S.; Bergès, J.; Mason, S. A.; Albinati, A.; Kozelka, J. Dispersion-Driven Hydrogen Bonding: Predicted Hydrogen Bond Between Water and Platinum(II) Identified by Neutron Diffraction. *Angew. Chem., Int. Ed.* **2010**, *49*, 7440−7443.
(19) Bergés, J.; Fourré, I.; Pilmé, J.; Kozelka, J. Quantum Chemical Topology Study of the Water-Platinum(II) Interaction. *Inorg. Chem.* **2013**, *52*, 1217−1227.
(20) Powles, J. The Structure of Molecular Liquids by Neutron Scattering. *Adv. Phys.* **1973**, *22*, 1−56.
(21) Soper, A. K.; Neilson, G. W.; Enderby, J. E.; Howe, R. A. A Neutron Diffraction Study of Hydration Effects in Aqueous Solutions. *J. Phys. C: Solid State Phys.* **1977**, *10*, 1793.
(22) Bowron, D. T.; Díaz-Moreno, S. Solvent Structure and the Extended Range Hydration of Cr^{3+} in Aqueous Solution. *J. Phys. Chem. B* **2009**, *113*, 11858−11864.
(23) Soper, A. K. Partial Structure Factors From Disordered Materials Diffraction Data: An Approach Using Empirical Potential Structure Refinement. *Phys. Rev. B* **2005**, *72*, 104204.
(24) Soper, A. Empirical Potential Monte Carlo Simulation of Fluid Structure. *Chem. Phys.* **1996**, *202*, 295−306.
(25) Soper, A. K. Partial Structure Factors From Disordered Materials Diffraction Data: An Approach Using Empirical Potential Structure Refinement. *Phys. Rev. B* **2005**, *72*, 104204.
(26) Biswas, P.; Atta-Fynn, R.; Drabold, D. A. Reverse Monte Carlo Modeling of Amorphous Silicon. *Phys. Rev. B* **2004**, *69*, 195207.
(27) Semrouni, D.; Wang, H.-W.; Clark, S. B.; Pearce, C. I.; Page, K.; Schenter, G.; Wesolowski, D. J.; Stack, A. G.; Clark, A. E. Resolving local configurational contributions to X-Ray and neutron radial distribution functions within solutions of concentrated electrolytes − a case study of concentrated NaOH. *Phys. Chem. Chem. Phys.* **2019**, *21*, 6828−6838.
(28) Hellquist, B.; Bengtsson, L. A.; Holmberg, B.; Hedman, B.; Persson, I.; Elding, L. I. Structures of Solvated Cations of Palladium(II) and Platinum(II) in Dimethyl Sulfoxide, Acetonitrile and Aqueous Solution Studied by EXAFS and LAXS. *Acta Chem. Scand.* **1991**, *45*, 449−455.
(29) Ayala, R.; Marcos, E. S.; Díaz-Moreno, S.; Solé, V. A.; Muñoz-Páez, A. Geometry and Hydration Structure of Pt(II) Square Planar Complexes $[Pt(H_2O)_4]^{2+}$ and $[PtCl_4]^{2-}$ as Studied by X-ray Absorption Spectroscopies and Quantum-Mechanical Computations. *J. Phys. Chem. B* **2001**, *105*, 7588−7593.
(30) Marx, D.; Hutter, J. *Ab Initio Molecular Dynamics: Basic Theory and Advanced Methods*; Cambridge University Press, 2009.
(31) Fonseca Guerra, C.; Snijders, J.; Te Velde, G. t.; Baerends, E. J. Towards an Order-N DFT Method. *Theor. Chem. Acc.* **1998**, *99*, 391−403.
(32) Fedorov, D. G. The Fragment Molecular Orbital Method: Theoretical Development, Implementation in GAMESS, and Applications. *WIREs Comput. Mol. Sci.* **2017**, *7*, e1322.
(33) Kitaura, K.; Ikeo, E.; Asada, T.; Nakano, T.; Uebayasi, M. Fragment Molecular Orbital Method: An Approximate Computational Method for Large Molecules. *Chem. Phys. Lett.* **1999**, *313*, 701−706.
(34) Wesolowski, T. A.; Shedge, S.; Zhou, X. Frozen-Density Embedding Strategy for Multilevel Simulations of Electronic Structure. *Chem. Rev.* **2015**, *115*, 5891−5928.
(35) Jacob, C. R.; Neugebauer, J. Subsystem Density-Functional Theory. *WIREs Comput Mol Sci* **2014**, *4*, 325−362.
(36) Jacob, C. R.; Visscher, L. A Subsystem Density-Functional Theory Approach for the Quantum Chemical Treatment of Proteins. *J. Chem. Phys.* **2008**, *128*, 04B612.
(37) Genova, A.; Ceresoli, D.; Krishtal, A.; Andreussi, O.; DiStasio, R. A., Jr.; Pavanello, M. eQE: An Open-source Densitiy Functional Embedding Theory Code For The Condensed Phase. *Int. J. Quantum Chem.* **2017**, *117*, e25401.
(38) Mi, W.; Shao, X.; Genova, A.; Ceresoli, D.; Pavanello, M. eQE 2.0: Subsystem DFT Beyond GGA Functionals. *Comput. Phys. Commun.* **2021**, *269*, 108122.
(39) Genova, A.; Ceresoli, D.; Pavanello, M. avoiding fractional electrons in subsystem DFT based ab-initio molecular dynamics yields accurate models for liquid water and solvated OH radical. *J. Chem. Phys.* **2016**, *144*, 234105.
(40) Mi, W.; Ramos, P.; Maranhao, J.; Pavanello, M. Ab initio Structure and Dynamics of CO_2 at Supercritical Conditions. *J. Phys. Chem. Lett.* **2019**, *10*, 7554−7559.
(41) Dasgupta, S.; Shahi, C.; Bhetwal, P.; Perdew, J. P.; Paesani, F. How Good Is the Density-Corrected SCAN Functional for Neutral and Ionic Aqueous Systems, and What Is So Right About the Hartree−Fock Density? *J. Chem. Theory Comput.* **2022**, *18*, 4745−4761. PMID: 35785808.
(42) Cococcioni, M.; De Gironcoli, S. Linear Response Approach to the Calculation of the Effective Interaction Parameters in the LDA+ U Method. *Phys. Rev. B* **2005**, *71*, 035105.
(43) Kulik, H. J.; Marzari, N. Systematic Study of First-Row Transition-Metal Diatomic Molecules: A Self-Consistent DFT+ U Approach. *J. Chem. Phys.* **2010**, *133*, 114103.
(44) Kulik, H. J.; Cococcioni, M.; Scherlis, D. A.; Marzari, N. Density Functional Theory in Transition-Metal Chemistry: A Self-Consistent Hubbard *U* Approach. *Phys. Rev. Lett.* **2006**, *97*, 103001.
(45) Zhao, Q.; Ioannidis, E. I.; Kulik, H. J. Global and Local Curvature in Density Functional Theory. *J. Chem. Phys.* **2016**, *145*, 054109.
(46) Krishtal, A.; Sinha, D.; Genova, A.; Pavanello, M. Subsystem Density-Functional Theory as an Effective Tool for Modeling Ground and Excited States, Their Dynamics and Many-Body Interactions. *J. Phys.: Condens. Matter* **2015**, *27*, 183202.
(47) Jacob, C. R.; Neugebauer, J. Subsystem Density-Functional Theory (Update). *WIREs Comput. Mol. Sci.* **2024**, *14*, e1700.
(48) Shao, X.; Lopez, A. C.; Khan Musa, M. R.; Nouri, M. R.; Pavanello, M. Adaptive Subsystem Density Functional Theory. *J. Chem. Theory Comput.* **2022**, *18*, 6646−6655.
(49) Luber, S. Sum Frequency Generation of Acetonitrile on a Rutile (110) Surface From Density Functional Theory-Based Molecular Dynamics. *J. Phys. Chem. Lett.* **2016**, *7*, 5183−5187.
(50) Luber, S. Local Electric Dipole Moments for Periodic Systems via Density Functional Theory Embedding. *J. Chem. Phys.* **2014**, *141*, 234110.
(51) VandeVondele, J.; Borštnik, U.; Hutter, J. Linear Scaling Self-Consistent Field Calculations With Millions of Atoms in the Condensed Phase. *J. Chem. Theory Comput.* **2012**, *8*, 3565−3573.
(52) Shao, X.; Mi, W.; Pavanello, M. Density Embedding Method for Nanoscale Molecule−Metal Interfaces. *J. Phys. Chem. Lett.* **2022**, *13*, 7147−7154.
(53) Shao, X.; Mi, W.; Pavanello, M. *eDFTpy: An Object-Oriented Platform for Density Embedding Simulations*. Available at http://edftpy.rutgers.edu 2021 (Last accessed on: 04/25/2024).
(54) Shao, X.; Andreussi, O.; Ceresoli, D.; Truscott, M.; Baczewski, A.; Campbell, Q.; Pavanello, M. *QEpy: Quantum ESPRESSO in*

https://doi.org/10.1021/acs.jpclett.4c00464
J. Phys. Chem. Lett. 2024, 15, 5517−5528

Python. 2021; https://gitlab.com/shaoxc/qepy (Last accessed on: 04/25/2024).
(55) Giannozzi, P.; Baroni, S.; Bonini, N.; Calandra, M.; Car, R.; Cavazzoni, C.; Ceresoli, D.; Chiarotti, G. L.; Cococcioni, M.; Dabo, I.; et al. Quantum ESPRESSO: A Modular and Open-Source Software Project for Quantum Simulations of Materials. *J. Phys.: Condens. Matter* **2009**, *21*, 395502.
(56) Dalcín, L.; Paz, R.; Storti, M. MPI for Python. *J. Parallel Distrib. Comput.* **2005**, *65*, 1108−1115.
(57) Laricchia, S.; Fabiano, E.; Constantin, L.; Della Sala, F. Generalized Gradient Approximations of the Noninteracting Kinetic Energy From the Semiclassical Atom Theory: Rationalization of the Accuracy of the Frozen Density Embedding Theory for Nonbonded Interactions. *J. Chem. Theory Comput.* **2011**, *7*, 2439−2451.
(58) Perdew, J. P.; Burke, K.; Ernzerhof, M. Generalized Gradient Approximation Made Simple. *Phys. Rev. Lett.* **1996**, *77*, 3865.
(59) Garrity, K. F.; Bennett, J. W.; Rabe, K. M.; Vanderbilt, D. Pseudopotentials for High-Throughput DFT Calculations. *Comput. Mater. Sci.* **2014**, *81*, 446−452.
(60) Chen, X.; Cifuentes-Lopez, A.; Shao, X.; Lin, L.; Prokopchuk, D.; Pavanello, M. Unraveling the Hydration Shell Structure and Dynamics of Group 10 Aqua Ions. *Zenodo* **2024**; DOI: 10.5281/zenodo.10654383.
(61) Housecroft, C. E.; Sharpe, A. G. *Inorganic Chemistry*, 5th ed.; Pearson Education Limited: London, 2018.
(62) Berendsen, H. J.; Postma, J. v.; Van Gunsteren, W. F.; DiNola, A.; Haak, J. R. Molecular Dynamics With Coupling to an External Bath. *J. Chem. Phys.* **1984**, *81*, 3684−3690.
(63) Frisch, M. J.; Trucks, G. W.; Schlegel, H. B.; Scuseria, G. E.; Robb, M. A.; Cheeseman, J. R.; Scalmani, G.; Barone, V.; Petersson, G. A.; Nakatsuji, H. et al. *Gaussian 16*, Rev. A.03; Gaussian Inc.: Wallingford, CT, 2016.
(64) Grimme, S.; Antony, J.; Ehrlich, S.; Krieg, H. A consistent and accurate ab initio parametrization of density functional dispersion correction (DFT-D) for the 94 elements H-Pu. *J. Chem. Phys.* **2010**, *132*, 154104.
(65) Caldeweyher, E.; Bannwarth, C.; Grimme, S. Extension of the D3 Dispersion Coefficient Model. *J. Chem. Phys.* **2017**, *147*, 034112.
(66) Caldeweyher, E.; Ehlert, S.; Hansen, A.; Neugebauer, H.; Spicher, S.; Bannwarth, C.; Grimme, S. A Generally Applicable Atomic-Charge Dependent London Dispersion Correction. *J. Chem. Phys.* **2019**, *150*, 154122.
(67) Caldeweyher, E.; Mewes, J.-M.; Ehlert, S.; Grimme, S. Extension and Evaluation of the D4 London-Dispersion Model for Periodic Systems. *Phys. Chem. Chem. Phys.* **2020**, *22*, 8499−8512.
(68) Ankudinov, A. L.; Ravel, B.; Rehr, J. J.; Conradson, S. D. Real-Space Multiple-Scattering Calculation and Interpretation of X-Ray-Absorption Near-Edge Structure. *Phys. Rev. B* **1998**, *58*, 7565−7576.
(69) Rehr, J. J.; Albers, R. C. Scattering-Matrix Formulation of Curved-Wave Multiple-Scattering Theory: Application to X-Ray-Absorption Fine Structure. *Phys. Rev. B* **1990**, *41*, 8139−8149.
(70) Brehm, M.; Thomas, M.; Gehrke, S.; Kirchner, B. TRAVIS—A Free Analyzer for Trajectories From Molecular Simulation. *J. Chem. Phys.* **2020**, *152*, 164105 DOI: 10.1063/5.0005078.
(71) Michaud-Agrawal, N.; Denning, E. J.; Woolf, T. B.; Beckstein, O. MDAnalysis: AToolkit for the Analysis of Molecular Dynamics Simulations. *J. Comput. Chem.* **2011**, *32*, 2319−2327.
(72) Gowers, R. J.; Linke, M.; Barnoud, J.; Reddy, T. J. E.; Melo, M. N.; Seyler, S. L.; Domański, J.; Dotson, D. L.; Buchoux, S.; Kenney, I. M.; et al. MDAnalysis: A Python Package for the Rapid Analysis of Molecular Dynamics Simulations. *Proceedings of the 15th Python in Science Conference* **2016**, 98−105.
(73) Humphrey, W.; Dalke, A.; Schulten, K. VMD − Visual Molecular Dynamics. *J. Mol. Graphics* **1996**, *14*, 33−38.
(74) Legault, C. Y. *CYLview20*; 2020; http://www.cylview.org (Last accessed on: 04/25/2024).
(75) Sandstrom, D. R. Ni^{2+} Coordination in Aqueous $NiCl_2$ Solutions: Study of the Extended X-Ray Absorption Fine Structure. *J. Chem. Phys.* **1979**, *71*, 2381−2386.
(76) Magini, M. Hydration and Complex Formation Study on Concentrated MCl_2 Solutions [M = Co(II), Ni(II), Cu(II)] by X-Ray Diffraction Technique. *J. Chem. Phys.* **1981**, *74*, 2523−2529.
(77) Neilson, G.; Enderby, J. E. The Structure of an Aqueous Solution of Nickel Chloride. *Proc. R. Soc. Lond. Ser. A. Mathematical and Physical Sciences* **1983**, *390*, 353−371.
(78) Soper, A.; Neilson, G.; Enderby, J.; Howe, R. A Neutron Diffraction Study of Hydration Effects in Aqueous Solutions. *J. Phys. C: Solid State Phys.* **1977**, *10*, 1793.
(79) Soper, A. K. The Structure of Aqueous Solutions. Ph.D. Thesis, University of Leicester, 1977.
(80) Neutron Scattering Lengths and Cross Sections. 2021; https://www.ncnr.nist.gov/resources/n-lengths/ (Last accessed on: 04/25/2024).
(81) Salacuse, J. J.; Denton, A. R.; Egelstaff, P. A. Finite-Size Effects in Molecular Dynamics Simulations: Static Structure Factor and Compressibility. I. Theoretical Method. *Phys. Rev. E* **1996**, *53*, 2382−2389.
(82) Herrero, C.; Pauletti, M.; Tocci, G.; Iannuzzi, M.; Joly, L. Connection Between Water's Dynamical and Structural Properties: Insights From Ab Initio Simulations. *Proc. Natl. Acad. Sci. U.S.A.* **2022**, *119*, e2121641119.
(83) Gillan, M. J.; Alfe, D.; Michaelides, A. Perspective: How Good Is DFT for Water. *J. Chem. Phys.* **2016**, *144*, 130901 DOI: 10.1063/1.4944633.
(84) Wang, L.-P.; McGibbon, R. T.; Pande, V. S.; Martinez, T. J. Automated Discovery and Refinement of Reactive Molecular Dynamics Pathways. *J. Chem. Theory Comput.* **2016**, *12*, 638−649.

https://doi.org/10.1021/acs.jpclett.4c00464
J. Phys. Chem. Lett. 2024, 15, 5517−5528